

Mitigating Residual Exchange Coupling in Resonant Singlet-Triplet Qubits

Jiheng Duan,^{1,2} Fernando Torres-Leal,^{1,2} and John M. Nichol^{1,2,*}

¹*Department of Physics and Astronomy, University of Rochester, Rochester, NY, 14627 USA*

²*University of Rochester Center for Coherence and Quantum Science, Rochester, NY, 14627, USA*

We propose methods to mitigate single- and two-qubit control errors due to residual exchange coupling in systems of exchange-coupled resonant singlet-triplet qubits. Commensurate driving, where the pulse length is an integer multiple of the drive period, can mitigate errors from residual intra-qubit exchange, including effects from counter rotating terms and off-axis rotations, as well as leakage errors during two-qubit operations. Residual inter-qubit exchange creates crosstalk errors that reduce single-qubit control fidelities. We show that using a single-spin coupler between two resonant singlet-triplet qubits can reduce this crosstalk error by an order of magnitude. Assuming perfect coupler state preparation and realistic charge and hyperfine noise, we predict that coupler-assisted two-qubit gate errors can be below 3×10^{-3} for gate times as short as 66 ns, even in the presence of residual exchange levels exceeding several hundred kHz. Our results suggest the potential of utilizing coupler-based architectures for large scale fault-tolerant spin qubit processors based on resonant singlet-triplet qubits.

I. INTRODUCTION

Spin qubits in semiconductor quantum dots [1] are promising physical qubits for fault-tolerant quantum processors [2–4], due to their long lifetimes [5–8], long-range spin shuttling [9–15], and the potential for high-density integration [16–23]. Recent experimental advances have demonstrated both single- and two-qubit gate fidelities exceeding 99% for single-spin-1/2 qubits [5, 24–26], reaching the threshold required for error correction using the surface code [27, 28]. Encoding quantum information in the joint state of more than one spin enables low-frequency control [17, 29–33], high-fidelity single-shot readout [33–38], and encoding in decoherence-free subspaces [39–42]. Singlet-triplet qubits based on two spins exemplify these potential advantages.

In the presence of a large magnetic-field gradient, the natural basis states of the singlet-triplet qubit are $|\uparrow\downarrow\rangle$ and $|\downarrow\uparrow\rangle$, forming the “flip-flop” or “resonant” singlet-triplet (RST) qubit [43, 44]. High-fidelity single-qubit control via oscillating exchange couplings, as well as initialization and readout via Pauli spin-blockade methods, have been demonstrated in RST qubits [45–50]. The $|\uparrow\downarrow\rangle, |\downarrow\uparrow\rangle$ basis is also the natural basis in which to consider a two-qubit gate based on the ZZ-interaction between exchange-coupled singlet-triplet qubits [51]. While the capacitive coupling has been employed to generate longitudinal inter-qubit interactions [46, 52], the exchange-based ZZ-interaction has not yet been conclusively demonstrated between singlet-triplet qubits [53].

However, nearly all spin qubits that utilize exchange coupling must contend with “residual exchange”, which results from the fact that exchange coupling between single electrons in separate dots is always positive [54]. In the context of RST qubits, this means that the basis states are not purely $|\uparrow\downarrow\rangle$ and $|\downarrow\uparrow\rangle$, and thus not or-

thogonal to the oscillating control field. In addition, this means that any oscillating exchange coupling is also accompanied by a non-zero time-averaged exchange. For two exchange-coupled RST qubits, the residual inter-qubit exchange creates a non-zero ZZ-interaction, causing quantum crosstalk errors in single-qubit gates on both qubits [24, 55]. This form of crosstalk, arising from the ZZ-interaction, is fundamentally different from microwave crosstalk between the driving electrodes of neighboring quantum dots [56–58].

Common approaches to mitigate effects of residual exchange include modifying the gate architecture or tuning to minimize the residual exchange. Typical residual exchange values using these approaches are on the order of a few hundred kilohertz, significantly suppressing quantum crosstalk [5, 24]. In these cases however, high-amplitude barrier-gate voltage pulses are required to turn on the exchange coupling between qubits. Such high-voltage pulses can disrupt the linear-regime gate virtualization, as described by the crosstalk matrix that captures capacitive coupling between all metallic gates [15, 21, 22, 59–61]. Previous studies have also suggested that such quantum crosstalk errors resulting from residual exchange can be suppressed by matching drive timings with Rabi periods and conditional precession frequencies [55]. By carefully synchronizing these time scales, residual-exchange-induced coherent errors can interfere destructively and cancel out. This approach enables improved gate fidelity without requiring complete suppression of the residual exchange coupling at the cost of additional gate complexity.

In this work, we propose a method to mitigate single-qubit errors in RST qubits from both residual intra- and inter-qubit exchange. By commensurately pulsing the intra-qubit exchange coupling at integer multiples the qubit Larmor period and compensating phase shifts with virtual-Z rotations [62], fast single-qubit gates with low coherent error can be achieved even in the presence of large residual intra-qubit exchange. To mitigate quantum crosstalk errors, we propose a single-spin coupler

* john.nichol@rochester.edu

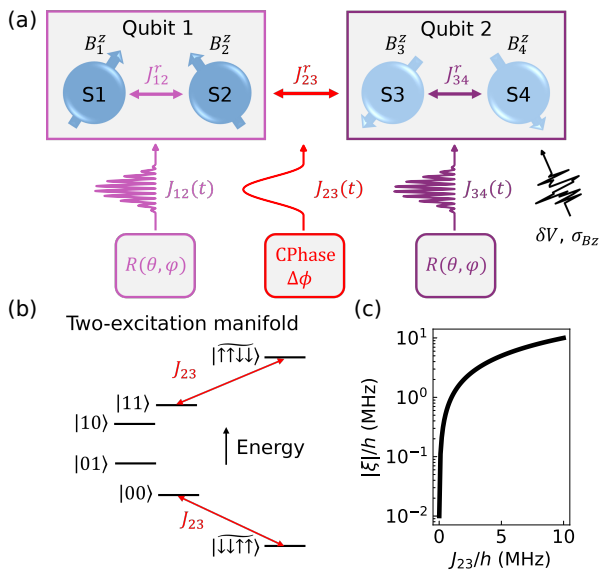


FIG. 1. (a) One-dimensional four-spin chain with spins $S1$ to $S4$. Two RST qubits are coupled through inter-qubit residual exchange J_{23}^r with individual intra-qubit residual exchange couplings J_{12}^r and J_{34}^r , respectively. Arbitrary single-qubit rotations can be realized by resonant intra-qubit exchange pulses together with virtual-Z gates. A CPhase gate can be achieved by pulsing inter-qubit exchange coupling. (b) Energy levels. The middle four levels and the remaining two levels span the computational and leakage subspaces, respectively. The inter-qubit exchange coupling J_{23} couples states between the two subspaces, causing leakage errors. (c) ZZ-interaction ζ vs. inter-qubit exchange coupling J_{23} .

between two RST qubits [63] to mediate a superexchange interaction [64] with large on-off ratios.

This paper is organized as follows. In Sec. II we discuss the Heisenberg exchange model of two coupled RST qubits in a one-dimensional spin chain [51]. Focusing on a single RST qubit, we derive the intra-qubit residual exchange-induced error under resonant driving without invoking the rotating-wave approximation (RWA) in Sec. III. The commensurate drive conditions are derived from the zeroth-order Magnus expansion of the time evolution operator for a $\pi/2$ rotation. The inter-qubit residual exchange-induced quantum crosstalk is discussed in Sec. IV. Quasi-state hyperfine noise and $1/f$ charge noise [65–68] are included to benchmark the performance of both $X_{\pi/2}$ and CZ gates. In Sec. IV, we propose a single-spin coupler architecture and evaluate all gate operations under a consistent noise environment.

II. SYSTEM AND MODEL

The RST qubit is constructed from the joint spin states of two electrons in a double quantum-dot in a large magnetic field gradient. In the absence of exchange coupling the eigenstates of the system are $\{|\downarrow\downarrow\rangle, |\downarrow\uparrow\rangle, |\uparrow\downarrow\rangle, |\uparrow\uparrow\rangle\}$.

In the presence of exchange coupling, the eigenstates of the system hybridize slightly, and we will refer to them in the following as $\{|\widetilde{\downarrow\downarrow}\rangle, |\widetilde{\downarrow\uparrow}\rangle, |\widetilde{\uparrow\downarrow}\rangle, |\widetilde{\uparrow\uparrow}\rangle\}$. The computational subspace of the RST qubit is spanned by the logical states $\{|0\rangle, |1\rangle\} = \{|\widetilde{\downarrow\uparrow}\rangle, |\widetilde{\uparrow\downarrow}\rangle\}$. Consider only the left RST qubit in Fig. 1(a), decoupled from the second qubit. The corresponding qubit Hamiltonian inside the logical subspace is

$$H_0 = -\frac{1}{2}\hbar\sqrt{\Delta\omega_{12}^2 + \left(\frac{J_{12}^r}{\hbar}\right)^2}\sigma_z, \quad (1)$$

where \hbar is the reduced Planck constant, $\Delta\omega_{12} = \omega_{s1} - \omega_{s2}$ is the spin Larmor frequency difference between spins S_1 and S_2 , J_{12}^r is the residual inter-qubit exchange, and σ_k , $k \in \{x, y, z\}$ is the Pauli operator.

Single-qubit control is achieved by resonantly pulsing the intra-qubit exchange coupling, illustrated both in Fig. 1(a) and Fig. 2(a). Modulating the carrier phase φ enables the implementation of virtual-Z gates and arbitrary single-qubit rotations $R(\theta, \varphi) = \exp[-i\theta(\cos\varphi\sigma_x - \sin\varphi\sigma_y)/2]$, as demonstrated in GaAs [46], Si [49], and Ge [50]. Because the exchange coupling between two electrons is non-negative, any control sequence that modulates the exchange also creates a non-zero residual exchange J^r . A non-zero residual exchange means that the quantization and control axes of the qubit are non-orthogonal and leads to pulse-dependent coherent errors, as discussed further in Sec. III.

Two-qubit gates are achieved by manipulating the exchange coupling between two RST qubits. Considering two exchange-coupled RST qubits in the presence of a large Zeeman gradient, illustrated in Fig. 1(a), the inter-qubit exchange coupling naturally creates a ZZ-interaction between two far-detuned spins. The energy levels of the two-excitation manifold are shown in Fig. 1(b) where the two-qubit computational subspace is spanned by $\{|00\rangle, |01\rangle, |10\rangle, |11\rangle\} = \{|\widetilde{\downarrow\uparrow\uparrow\downarrow}\rangle, |\widetilde{\downarrow\uparrow\downarrow\uparrow}\rangle, |\widetilde{\uparrow\downarrow\uparrow\downarrow}\rangle, |\widetilde{\uparrow\downarrow\downarrow\uparrow}\rangle\}$. Such a ZZ-interaction between spins from two RST qubits induces an effective ZZ-interaction in the two-qubit computational subspace. The strength of the coupling is defined as [69]

$$\zeta = E_{11} + E_{00} - E_{10} - E_{01}, \quad (2)$$

where E_{kl} is the eigenenergy of the two-qubit eigenstate $|k, l\rangle$ for $k, l \in \{0, 1\}$. Fig. 1(c) shows the ZZ-interaction against the inter-qubit exchange coupling J_{23} . The inter-qubit exchange coupling, however, also induces leakage out of the computational subspace. The leakage subspace is spanned by $\{|\widetilde{\uparrow\uparrow\downarrow\downarrow}\rangle, |\widetilde{\downarrow\downarrow\uparrow\uparrow}\rangle\}$ and is connected to the computational subspace through inter-qubit exchange coupling J_{23} . Methods such as adiabatic pulse shaping have been proposed to suppress leakage errors [51].

In the following, we will explore the effects of residual exchange on RST qubits with analytical and numerical

approaches. To numerically simulate the behavior of coupled RST qubits, we consider a complete four-spin chain, with Hamiltonian

$$H_s = -\frac{1}{2} \sum_{k=1}^4 \hbar \omega_{s,k} s_k^z + \frac{1}{4} \sum_{k=1}^3 J_{k,k+1}^r \vec{s}_k \cdot \vec{s}_{k+1}. \quad (3)$$

Here $\hbar \omega_{s,k} = g_k \mu_B B_k^z$ is the Zeeman energy, g_k is the gyromagnetic ratio, μ_B is the Bohr magneton, and B_k^z ($k = 1, \dots, 4$) is the local magnetic field in z-direction, s_k^μ is the Pauli operator of the decoupled spins, and $\vec{s}_k = (s_k^x, s_k^y, s_k^z)$. The residual exchange couplings between spins within the same qubit and those connecting different qubits are referred to as intra-qubit (J_{12}^r, J_{34}^r) and inter-qubit (J_{23}^r) residual exchange, respectively.

In our simulations we assume that exchange is controlled by pulsing the effective inter-dot tunnel barrier gate voltage $V_B(t)$. It can be modeled as [5, 24, 70, 71]

$$J(t) = J^r e^{2\alpha V_B(t)}, \quad (4)$$

where J^r is the residual exchange coupling and $\alpha = 0.011 \text{ mV}^{-1}$ is an empirical lever arm. We numerically simulate the evolution of the four-spin system under the influence of time-dependent exchange couplings using QuTiP [72, 73]. To extract information about the individual RST qubits, we compute the partial traces of the overall density matrix. Table I lists the simulation parameters we use.

In our simulations, unless stated otherwise, we also include the effects of both charge noise and hyperfine noise. To include the effects of stochastic noise, we perform Monte Carlo simulations in which each result is averaged over 512 realizations. We include charge noise by generating a noise time series with a $1/f$ power spectral density (PSD)

$$S_{V_B}(f) = \frac{A_\mu^2 \gamma^{-2}}{f}, \quad (5)$$

where $A_\mu = 1 \text{ } \mu\text{eV}$ is the PSD amplitude at 1 Hz, and $\gamma = 0.1 \text{ eV/V}$ is the lever arm [65, 67, 74]. Details of the charge noise simulations are discussed in Appendix D. We note that the voltage noise associated with the barrier becomes dominant at high exchange coupling as its sensitivity exponentially grows with the barrier voltage:

$$\frac{\partial J}{\partial V_B} = 2\alpha J^r e^{2\alpha V_B}. \quad (6)$$

This fact has important implications for RST gate fidelities, as discussed further below.

For spin k , the contribution from hyperfine noise is formulated as a stochastic offset on its Larmor frequency $\omega_{s,k} + \delta\omega_{s,k}$. The hyperfine noise term $\delta\omega_{s,k}$ is considered as quasi-static and its amplitude is described by the standard deviation σ_{Bz} of its Gaussian distribution $\delta\omega_{s,k} \sim \mathcal{N}(0, \sigma_{Bz}^2)$ with zero mean. Here we use hyperfine noise with amplitude $\sigma_{Bz} = 2\pi \times 0.05 \text{ MHz}$, which corresponds to a simulated single-spin Ramsey coherence time $T_2^* \approx 2.37 \text{ } \mu\text{s}$. Further details about hyperfine noise are discussed in Appendix E.

TABLE I. Default simulation parameters

Parameter	Value
$\omega_{s1}/2\pi$	10.75 GHz
$\omega_{s2}/2\pi$	10.60 GHz
$\omega_{s3}/2\pi$	10.48 GHz
$\omega_{s4}/2\pi$	10.35 GHz
$\omega_{sc}/2\pi$	10.54 GHz
$J_{12}^r/\hbar, J_{23}^r/\hbar$	2 MHz
$J_{2c}^r/\hbar, J_{3c}^r/\hbar$	12 MHz
γ	0.1 eV/V
α	0.011 mV ⁻¹
A_μ	1 $\mu\text{eV}/\sqrt{\text{Hz}}$
$\sigma_{Bz}/2\pi$	0.05 MHz

III. INTRA-QUBIT RESIDUAL EXCHANGE

A. Single-qubit gate error

We begin by considering the effects of residual exchange within one qubit, which we refer to as intra-qubit residual exchange. To illustrate the effects of intra-qubit residual exchange, consider only the left RST qubit in Fig. 1(a), decoupled from the second qubit and subjected to a resonant exchange drive. We split the RST qubit Hamiltonian into two parts: the static part H_0 , which includes J_{12}^r , and the drive part $H_d(t)$, which includes the total exchange coupling $J_{12}(t)$ minus the static residual part. (Further details can be found in Appendix A.) The total Hamiltonian is:

$$H(t) = H_0 + H_d(t), \quad (7)$$

$$H_0 = -\frac{1}{2} \hbar \omega_q \sigma_z, \quad (8)$$

$$H_d(t) = \frac{1}{2} [J_{12}(t) - J_{12}^r] (\cos \Theta \sigma_x - \sin \Theta \sigma_z), \quad (9)$$

where $\omega_q = \sqrt{(\omega_{s1} - \omega_{s2})^2 + (J_{12}^r/\hbar)^2}$ is the qubit frequency, J_{12}^r is the intra-qubit residual exchange coupling, and Θ is the angle between the quantization and exchange axes, i.e., $\cos \Theta = |\omega_{s1} - \omega_{s2}|/\omega_q$ and $\sin \Theta = J_{12}^r/\hbar \omega_q$.

We choose a logarithmic cosine envelope for the drive pulse [75]. Fig. 2(a) shows such a voltage pulse and the associated exchange pulse, which takes the form

$$J_{12}(t) = J_{12}^r + J_d s(t) [1 + \cos(\omega_d t + \varphi)], \quad (10)$$

where J_d is the amplitude, ω_d is the carrier frequency, φ is the carrier phase, and $s(t)$ is the cosine envelope. For a fixed pulse width τ , we choose the envelope function as

$$s(t) = \frac{1}{2} - \frac{1}{2} \cos\left(\frac{2\pi t}{\tau}\right). \quad (11)$$

We analyze the dynamics by transforming into the rotating frame with respect to the drive frequency. When

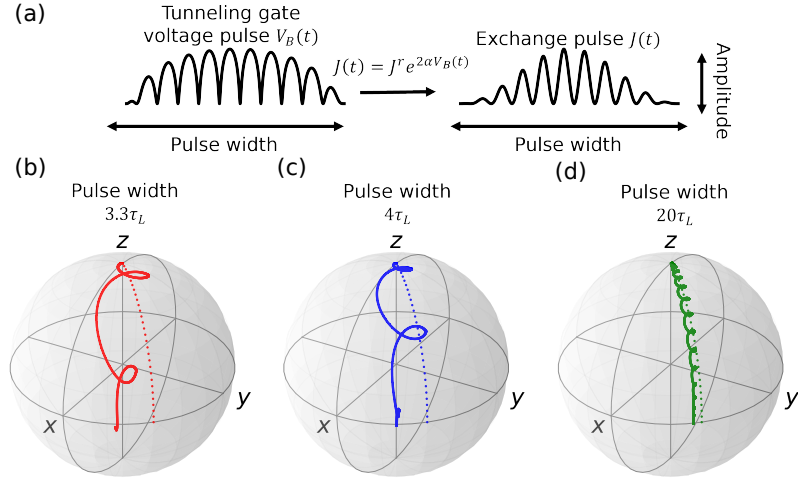


FIG. 2. (a) An inter-dot tunneling-gate voltage pulse with a logarithmic-cosine envelope can generate an exchange pulse with a cosine envelope. (b)-(d) Trajectory on the Bloch sphere during a $\pi/2$ rotation with phase $\pi/4$, illustrated in solid lines. The corresponding dashed lines are the ideal rotations. The pulse width at each case is (b) $3.3\tau_L$, (c) $4\tau_L$, and (d) $20\tau_L$. An unfinished fast rotation for $3.3\tau_L$ is observed.

$\omega_d = \omega_q$, the effective Hamiltonian becomes

$$H_{\text{eff}}(t) = \frac{1}{4}J_d s(t) \cos \Theta \begin{bmatrix} 0 & e^{i\varphi} \\ e^{-i\varphi} & 0 \end{bmatrix} + H_\varepsilon(t). \quad (12)$$

Here i is the imaginary unit, and H_ε is the error matrix, formulated by

$$H_\varepsilon(t) = \begin{bmatrix} -\varepsilon_z(t) & \varepsilon_x(t) \\ \varepsilon_x^\dagger(t) & \varepsilon_z(t) \end{bmatrix}, \quad (13)$$

where the matrix elements $\varepsilon_x(t)$ and $\varepsilon_z(t)$ are

$$\varepsilon_x(t) = \frac{1}{4}J_d s(t) \cos \Theta \left[2e^{-i\omega_d t} + e^{-i(2\omega_d t + \varphi)} \right], \quad (14)$$

$$\varepsilon_z(t) = \frac{1}{2}J_d s(t) \sin \Theta \left[1 + \cos(\omega_d t + \varphi) \right]. \quad (15)$$

Equations (12)-(15) suggest that any drive through the intra-qubit exchange leads to unwanted rotations about both the x and z axes, resulting pulse-dependent coherent errors. In particular, since exchange coupling is always positive, the non-zero time averaged value of the exchange drive will result in unwanted rotations around the z -axis, as well as a drive in the rotating frame at frequency ω_d . The usual counter-rotating terms at frequency $2\omega_d$ also appear and can create errors if the drive amplitude becomes comparable to the drive frequency (typically hundreds of MHz in RST qubits). Similar effects have been reported in superconducting fluxonium qubits [76, 77], whose transition frequency between the ground and the first excited state is less than 1 GHz.

B. Commensurate drive

Equations (14) and (15) indicate that the error terms oscillate at integer multiples of the drive frequency. This

fact suggests that the effects of the errors can be mitigated by choosing gate times at integer multiples of the Larmor period. To explore this possibility, we simulate the RST qubit formed from spins 1 and 2 undergoing a resonant drive with the parameters listed above. Figs. 2(b)-(d) illustrate the trajectories of the Bloch vector $\vec{r} = (r_x, r_y, r_z)$ during a $R(\pi/2, \pi/4)$ rotation for different gate times, where $\tau_L = 2\pi/\omega_q$ is the Larmor period. Solid lines represent the actual rotations coming from the resonant single-qubit drives shown in Fig. 2(a), while dashed lines indicate the ideal trajectories. The fast oscillatory motion observed in all cases arises from counter-rotating effects and the presence of positive residual exchange. The $3.3\tau_L$ trajectory ends off the equator due to incomplete fast rotations. In contrast, for pulse durations of $4\tau_L$ and $20\tau_L$, the trajectories terminate properly on the equator. This behavior at integer multiples of the Larmor period occurs because the counter-rotating and positive-exchange errors, represented by $\varepsilon_x(t)$, destructively interfere with themselves at end of each full Larmor cycle. Unwanted phase accumulation is evident in all cases, highlighting the presence of the off-axis rotation error, described by $\varepsilon_z(t)$.

To explore this in more detail, we consider the unitary time evolution operator of the effective Hamiltonian in Eq. (12) under an exchange pulse with pulse width τ :

$$U(\tau) = \mathcal{T} \exp \left[-\frac{i}{\hbar} \int_0^\tau dt H_{\text{eff}}(t) \right], \quad (16)$$

where \mathcal{T} is the time-ordering operator. Expanding $U(\tau)$ using the Magnus expansion [78] and retaining only the zeroth-order term yields

$$U^{(0)}(\tau) = \exp \left[-\frac{i}{\hbar} \int_0^\tau dt H_{\text{eff}}(t) \right]. \quad (17)$$

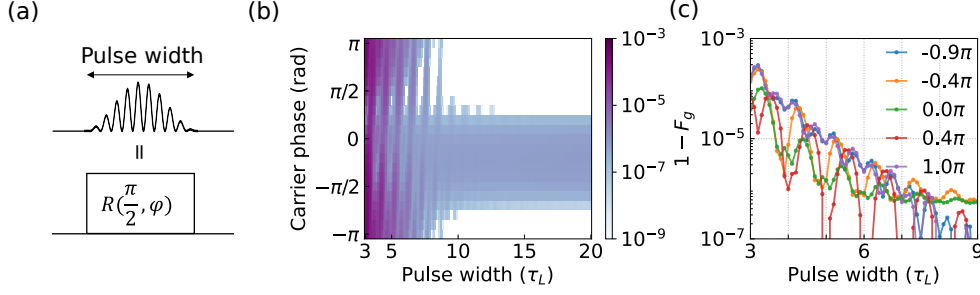


FIG. 3. Single-qubit gate for a RST qubit with intra-qubit residual exchange coupling $J_{\text{intra}}^r/\hbar = 2\pi \times 2$ MHz. (a) Exchange pulse waveform with carrier phase φ driving a qubit $\pi/2$ -rotation $R(\pi/2, \varphi)$. (b) Coherent error of the $\pi/2$ rotation for different carrier phases and pulse widths. (c) Horizontal traces from panel (b) at different carrier phases. Local minima of the gate infidelity occur when the pulse width is an integer multiple of the Larmor period.

We define the error integrals as

$$I_k = \frac{1}{\hbar} \int_0^\tau dt \varepsilon_k(t), \quad (18)$$

where $k \in \{x, z\}$. The integral of the envelope function [Eq. (11)], is $\int_0^\tau dt s(t) = \tau/2$. With these considerations, the unitary operator is then

$$U^{(0)}(\tau) = \begin{bmatrix} \cos \frac{\theta}{2} - i \frac{\theta_3}{\theta} \sin \frac{\theta}{2} & -\frac{\theta_2 + i\theta_1}{\theta} \sin \frac{\theta}{2} \\ \frac{\theta_2 - i\theta_1}{\theta} \sin \frac{\theta}{2} & \cos \frac{\theta}{2} + i \frac{\theta_3}{\theta} \sin \frac{\theta}{2} \end{bmatrix}, \quad (19)$$

where

$$\theta_1 = \frac{1}{4\hbar} J_d \tau \cos \Theta \cos \varphi + 2 \text{Re}\{I_x\}, \quad (20)$$

$$\theta_2 = -\frac{1}{4\hbar} J_d \tau \cos \Theta \sin \varphi - 2 \text{Im}\{I_x\}, \quad (21)$$

$$\theta_3 = -2I_z, \quad (22)$$

and $\theta = \sqrt{\theta_1^2 + \theta_2^2 + \theta_3^2}$. Notice that $U^{(0)}(\tau)$ represents an arbitrary ideal transversal rotation $R(\theta, \varphi)$ when both the error integrals approach zero. By doing the integrals I_x and I_z :

$$I_x = \frac{\pi^2 J_d \cos \Theta (1 - e^{-i\omega_d \tau})}{16i\hbar\omega_d} \times \left[\frac{e^{-i\varphi} (1 + e^{-i\omega_d \tau})}{\pi^2 - \omega_d^2 \tau^2} + \frac{16}{4\pi^2 - \omega_d^2 \tau^2} \right], \quad (23)$$

and

$$I_z = \frac{\pi^2 J_d \sin \Theta}{\hbar\omega_d} \times \left[\frac{\omega_d \tau}{4\pi^2} + \frac{\sin(\omega_d \tau + \varphi) - \sin \varphi}{4\pi^2 - \omega_d^2 \tau^2} \right], \quad (24)$$

one can notice that when $\omega_d \tau = 2n\pi$ for $n \in \mathbb{Z}^+$, $I_x = 0$ and I_z becomes independent of φ . The results suggest that when driving on resonance at the qubit frequency, all coherent errors can be minimized at zeroth order in the Magnus expansion by choosing the pulse duration

to be an integer multiple of the qubit Larmor period, $\tau = n\tau_L$, known as commensurate driving [76, 79]. Notice that this technique also works when driving with a detuning, i.e., $\omega_d - \omega_q \neq 0$, where additional Z-rotations will occur and can be mitigated by modifying the virtual-Z compensations later.

C. Single-qubit gate fidelity

To assess the reduction in single-qubit gate errors with commensurate driving, we compute an average gate fidelity based on simulations in the absence of noise (see the following section for fidelity estimates in the presence of noise and Appendix F for more details). The $R(\pi/2, \varphi)$ gate fidelity implemented by the unitary evolution $U(\tau)$ in Eq. (19) is

$$F_g = \frac{1}{3} (2F_e + 1), \quad (25)$$

where F_e is the entanglement fidelity, calculated by

$$F_e = \frac{1}{4} \sum_{\rho \in \{\rho_0\}} \text{Tr}[\rho_\tau(\rho) \rho_{\text{ideal}}(\rho)]. \quad (26)$$

Here, $\rho_\tau(\rho) = U(\tau)\rho U^\dagger(\tau)$ and $\rho_{\text{ideal}}(\rho) = R(\pi/2, \varphi)\rho R(-\pi/2, \varphi)$ denotes the states produced by the actual and ideal evolutions acting on the initial state ρ , respectively. The set of single-qubit fiducial states is $\{\rho_0\} = \{|0\rangle, |1\rangle, (|0\rangle + |1\rangle)/\sqrt{2}, (|0\rangle + i|1\rangle)/\sqrt{2}\}$. Fig. 3(b) shows the coherent error with varying pulse width and carrier phase, where the diagrammatic pulse sequence is illustrated in Fig. 3(a). The gate error becomes lower at longer pulse widths as smaller pulse amplitudes are required. Fig. 3(c) illustrates the gate error against pulse width with different carrier phase φ . The gate error reaches a local minimum around each integer multiple of the qubit Larmor frequency, consistent with our expectations for commensurate driving. Fig. 4(a) shows the coherent error against pulse width under commensurate drive with different intra-qubit

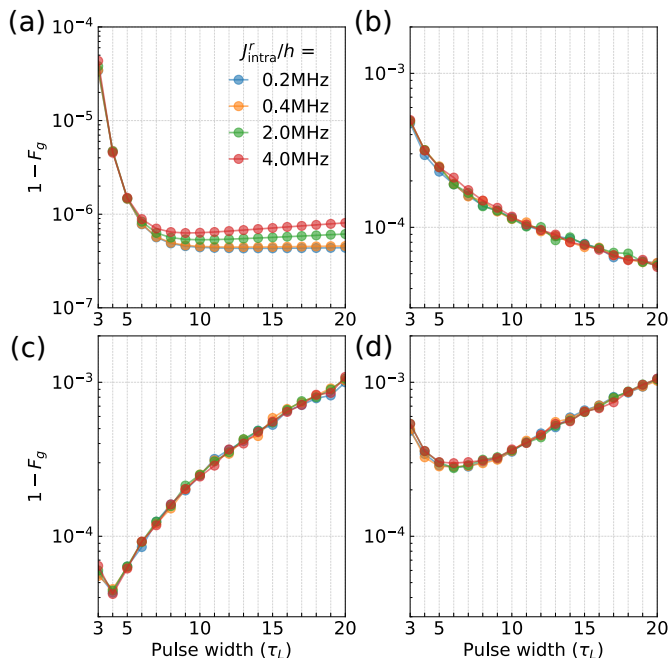


FIG. 4. Error budget of a commensurately-driven $\pi/2$ gate. (a) Coherent error. (b) Charge noise error. (c) Hyperfine noise error. (d) All errors.

residual exchange values. There is minimal dependence of the error on the intra-qubit residual exchange coupling, suggesting the robustness of the commensurate drive technique against residual exchange.

D. Error budget of a noisy $X_{\pi/2}$ gate

To evaluate how well commensurate driving works in the presence of electrical and hyperfine fluctuations, we evaluate single-qubit $X_{\pi/2}$ gate fidelities with different noise configurations. Figs. 4(b)-(d) show Monte Carlo simulations of the commensurate $X_{\pi/2}$ gate fidelity against pulse width with only charge noise, hyperfine noise, and both, respectively. The errors from charge noise decrease with the pulse length, because longer pulse widths require smaller exchange pulse amplitudes, reducing the sensitivity to charge noise. Conversely, with only hyperfine noise, the errors increase with pulse width due to increased effects of hyperfine dephasing during longer pulses. No significant variations in charge- or hyperfine-induced errors are observed across different values of intra-qubit residual exchange J_{intra}^r . When both charge and hyperfine noise are included, an optimum configuration around $6\tau_L$ emerges due to the competing effects of charge and hyperfine noise. These results suggest that, with commensurate driving, coherent errors arising from J_{intra}^r can be effectively mitigated under realistic noise conditions.

IV. INTER-QUBIT RESIDUAL EXCHANGE

A. Error budget of a noisy CZ gate

We now turn to the effects of residual exchange between qubits, or inter-qubit residual exchange. As discussed above, two RST qubits interacting via inter-qubit exchange experience a ZZ-interaction, as described by Eq. (2). This interaction naturally leads to a two-qubit CZ gate, which can be implemented by pulsing the inter-qubit exchange coupling. As discussed above, pulsing the inter-qubit exchange can lead to leakage outside the computational subspace, which can be partially mitigated by adiabatic pulse shaping [51, 80].

Similar to single-qubit commensurate driving, one can also mitigate the leakage dynamics by carefully controlling the CZ gate pulse width. The two-qubit dynamics in the presence of inter-qubit residual exchange coupling can be characterized with a time scale specific to the coupling strength to each of the leakage states. We define this timescale as

$$\tau_{CZ} = \frac{h}{|E_{\uparrow\uparrow\downarrow\downarrow} - E_{00}| + |E_{\downarrow\downarrow\uparrow\uparrow} - E_{11}|}. \quad (27)$$

A CZ gate implemented by a process $U_{CZ}(\tau)$ with pulse width τ is considered to be commensurately driven when the pulse width is an integer multiple of τ_{CZ} .

To demonstrate this possibility in simulation, we simulate a two-qubit CZ gate and calculate the fidelity with

$$F_{CZ} = \frac{1}{5} (4F_e^{CZ} + 1), \quad (28)$$

where the two-qubit entanglement fidelity is given by

$$F_e^{CZ} = \frac{1}{16} \sum_{\rho \in \{\rho'_0\}} \text{Tr}[\rho_\tau(\rho) \rho_{\text{ideal}}(\rho)]. \quad (29)$$

Here $\rho_\tau(\rho) = U_{CZ}(\tau)\rho U_{CZ}^\dagger(\tau)$, $\rho_{\text{ideal}}(\rho) = CZ\rho CZ$ is the ideal evolution of initial state ρ , and $\{\rho'_0\} = \{\rho_A \otimes \rho_B\}$ for $\rho_A, \rho_B \in \{|0\rangle, |1\rangle, (|0\rangle + |1\rangle)/\sqrt{2}, (|0\rangle + i|1\rangle)/\sqrt{2}\}$ is a set of two-qubit fiducial states.

Fig. 5(a) shows the CZ gate error with charge noise versus pulse width and hyperfine noise strength. The non-monotonic dependence of the error on the pulse width, observed when the hyperfine noise strength exceeds $2\pi \times 0.05$ MHz, results from the dominant error mechanism shifting from leakage dynamics to hyperfine noise. Fig. 5(b) shows the CZ gate errors under both charge and hyperfine noise, with $\sigma_{Bz} = 2\pi \times 0.04$ MHz, plotted against pulse width and inter-qubit residual exchange coupling strength. No significant variation is observed across different values of inter-qubit residual exchange, suggesting the effectiveness of commensurate driving at mitigating leakage errors. Fig. 5(c) shows the population in the leakage states $|\uparrow\uparrow\downarrow\downarrow\rangle$, and $|\downarrow\downarrow\uparrow\uparrow\rangle$, the total population outside the computational subspace,

and the coherent error, all illustrated as the pulse length varies, and without noise. As the pulse width increases, all error sources become less significant, and gate performance eventually becomes limited primarily by hyperfine noise. An oscillating pattern of the errors in Fig. 5(c) between interleaved even and odd time steps appears due to residual calibration errors, which cancel out after an even number of leakage-dynamics periods.

B. Single-qubit control crosstalk

A more serious challenge associated with residual inter-qubit exchange, however, arises from the fact that the exchange coupling cannot be made zero. Residual inter-qubit exchange leads to a quantum crosstalk effect, which depends on the residual ZZ-interaction strength ζ , and where the transition frequency of one qubit becomes dependent on the state of the other qubit.

To illustrate this effect, we simulate the behavior of two RST qubits as listed in Table I and assume commensurate driving. We focus on the single-qubit $X_{\pi/2}$ gate of the first qubit, where the system is initialized in $|\downarrow\uparrow\downarrow\uparrow\rangle$. Fig. 5(d) shows the single-qubit $X_{\pi/2}$ gate error on the first qubit against inter-qubit residual exchange $J_{\text{inter}}^r = J_{23}^r$ and hyperfine noise amplitude σ_{Bz} . Once the residual exchange coupling exceeds the hyperfine noise amplitude, the gate error increases dramatically as a result of the crosstalk effect. For isotopically pure silicon, where the hyperfine noise is $\sigma_{Bz} = 2\pi \times 0.04$ MHz [24], gate errors below 1×10^{-3} , require residual exchange values less than approximately 0.12 MHz.

C. Single-spin coupler

One approach to mitigating this crosstalk error is to design the device with a large dynamic range such that the exchange pulse can be sufficiently small at low gate voltages to minimize the crosstalk but simultaneously large enough at high gate voltages to implement rapid logic gates. Another approach, which we now discuss, involves introducing a single spin as a coupler between two RST qubits.

Consider two RST qubits, each connected to a central coupler spin, as illustrated in Fig. 6(a). The coupler spin S_C experiences a local magnetic field B_c^z and is exchange-coupled to two qubit spins S_2 and S_3 . The spin-coupler system Hamiltonian is then

$$H_{sc} = -\frac{1}{2} \sum_{k=1}^4 \hbar \omega_{s,k} s_k^z + \frac{1}{4} \sum_{k=1,3} J_{k,k+1}^r \vec{s}_k \cdot \vec{s}_{k+1} - \frac{1}{2} \hbar \omega_{s,c} s_c^z + \frac{1}{4} \sum_{k=2,3} J_{k,c}^r \vec{s}_k \cdot \vec{s}_c, \quad (30)$$

where $\hbar \omega_{s,k} = g_k \mu_B B_k^z$ is the Zeeman energy of spin ($k \in \{1, 2, 3, 4, c\}$), J_{12}^r and J_{34}^r are intra-residual ex-

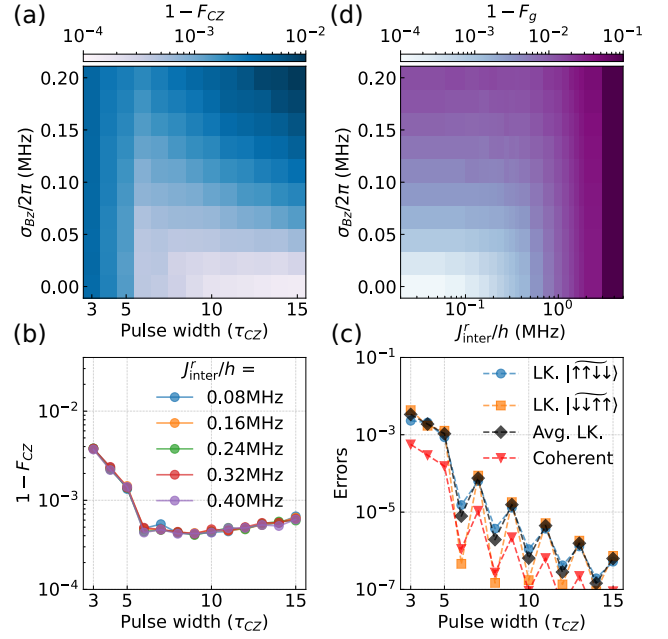


FIG. 5. $X_{\pi/2}$ and CZ gate error of two exchanged-coupled RST qubits. (a) CZ gate error with different pulse widths and hyperfine noise amplitudes with $J_{23}^r/h = 0.4$ MHz. (b) CZ gate error with $\sigma_{Bz} = 2\pi \times 0.04$ MHz and varying pulse widths and inter-qubit residual exchange values. (c) Leakage and coherent error budget of a CZ gate with $J_{23}^r/h = 0.4$ MHz. (d) $X_{\pi/2}$ gate error with different inter-qubit residual exchange coupling $J_{\text{inter}}^r = J_{23}^r$ and hyperfine noise amplitudes. The gate time used here is $10\tau_L$.

change coupling, J_{2c}^r and J_{3c}^r are inter-qubit residual exchange coupling.

In the remainder of the section, we consider a symmetric exchange coupling between each qubit-coupler spin pair, i.e., $J_{2c}^r = J_{3c}^r$. The computational subspace is defined as $\{|00\rangle, |01\rangle, |10\rangle, |11\rangle\} = \{|\downarrow\uparrow\downarrow\uparrow\rangle, |\downarrow\uparrow\uparrow\downarrow\rangle, |\uparrow\downarrow\downarrow\uparrow\rangle, |\uparrow\downarrow\uparrow\downarrow\rangle\}$. The eigenstates are labeled by $|S_1 S_2 S_3 S_4 S_C\rangle$, where the qubit-spin and coupler-spin are in single and double arrows, respectively. The coupler spin remains in its ground state during normal operation.

We model our spin chain with spin frequency consecutively decreasing from S_1 to S_4 , yielding an energy-level diagram inside the two-excitation manifold as shown in Fig. 6(b). The states on the left and right sides represent the computational and leakage states, respectively. In contrast to the scenario without a coupler, leakage errors now occur in general only when the coupler is excited. Thus, the leakage channels discussed previously no longer appear at first order because of the introduction of the coupler.

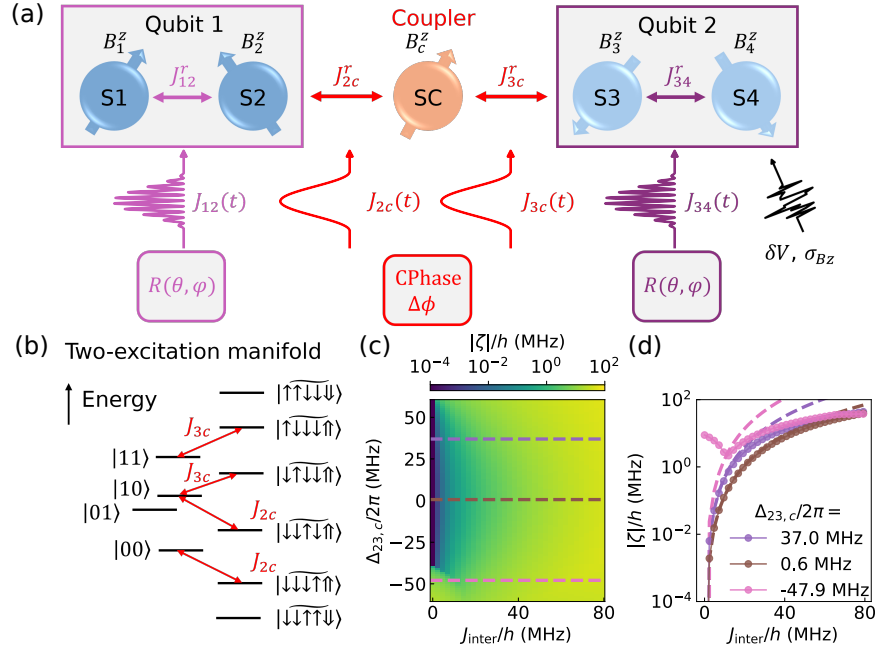


FIG. 6. (a) One-dimensional spin chain with five electrons where the middle spin serves as a coupler between two RST qubits. (b) Energy levels of the two-excitation manifold. The four levels on the left and the six levels on the right form the computational and leakage subspaces, respectively. (c) ZZ-interaction ζ extracted by diagonalizing Eq. (30) at different coupler frequencies ω_{sc} and inter-qubit residual exchange values J_{inter} . The qubit-spin frequencies and intra-qubit residual exchange are as in Table I. (d) Horizontal cuts from (c). The dashed lines are the corresponding perturbation results from Eq. (31).

1. ZZ-interaction

For large qubit-spin/coupler-spin Larmor-frequency detuning Δ_{kc} , the effective ZZ-interaction between RST qubits is (see Appendix C):

$$\zeta \approx -\frac{J_{2c}J_{3c}}{4\hbar^2} \left(\frac{J_{2c}}{\Delta_{2c}^2} + \frac{J_{3c}}{\Delta_{3c}^2} \right), \quad (31)$$

where $\Delta_{kc} = |\omega_{s,k} - \omega_{s,c}|$ for $k \in \{2, 3\}$. Maximizing the on-off-ratio of the ZZ-interaction requires that $\omega_{s3} - \omega_{sc} = \omega_{sc} - \omega_{s2}$, i.e., $\Delta_{23,c} = 0$, where

$$\Delta_{23,c} = \omega_{sc} - \frac{\omega_{s2} + \omega_{s3}}{2}. \quad (32)$$

Fig. 6(c) shows the ZZ-interaction for varying coupler frequency and inter-qubit exchange coupling. Fig. 6(d) shows horizontal traces with varying coupler frequencies, where the solid and dashed lines are data extracted from (c) and the corresponding analytical solutions from Eq. (31), respectively.

Since the residual ZZ-interaction arising from residual exchange coupling is quadratically suppressed by the frequency detuning between the qubit and coupler spins, a significant reduction in single-qubit gate crosstalk is expected. Fig. 7(a) compares the single-qubit gate error for the direct coupling case and the midpoint-frequency coupler configuration ($\Delta_{23,c} = 0$). The pulse width for the single-qubit gate is set to $15\tau_L$ in this analysis. We

observe a two-order-of-magnitude reduction in coherent errors with the coupler, even at small inter-qubit residual exchange values. The coupler shows a tolerance of residual exchange up to 4 MHz. Even at such high inter-qubit exchange coupling values, the ZZ-interaction reaches $2\pi \times 10$ MHz, with an on-off ratio on the order of 10^4 with respect to the residual level. We expect that pulsing exchange couplings between both qubit-coupler spins to around 60 MHz will enable a CZ gate with a duration of tens to hundreds of nanoseconds.

2. Error budget of noisy $X_{\pi/2}$ and CZ gates with a coupler

In the following discussion we assume the coupler can be perfectly initialized on its ground state. The single-qubit $X_{\pi/2}$ gate error with varying inter-qubit residual exchange J_{inter}^r and hyperfine noise values σ_{Bz} is illustrated in Fig. 7(b). In contrast to the results shown in Fig. 5, the coherent error when $\sigma_{Bz} = 2\pi \times 0.04$ MHz remains small up to residual exchange values up to around 10 MHz. This robustness to residual exchange illustrates the potential of the spin coupler.

Turning to the CZ gate error, we set a large residual exchange value and $J_{\text{inter}}^r/h = 12$ MHz. Fig. 7(c) shows the coupler-assisted CZ gate error plotted against the CZ gate pulse width and hyperfine noise level. Similar to the directly-coupled case in Eq. (27), the unit cycle time τ_{CZ} for commensurate driving is based on the inverse of

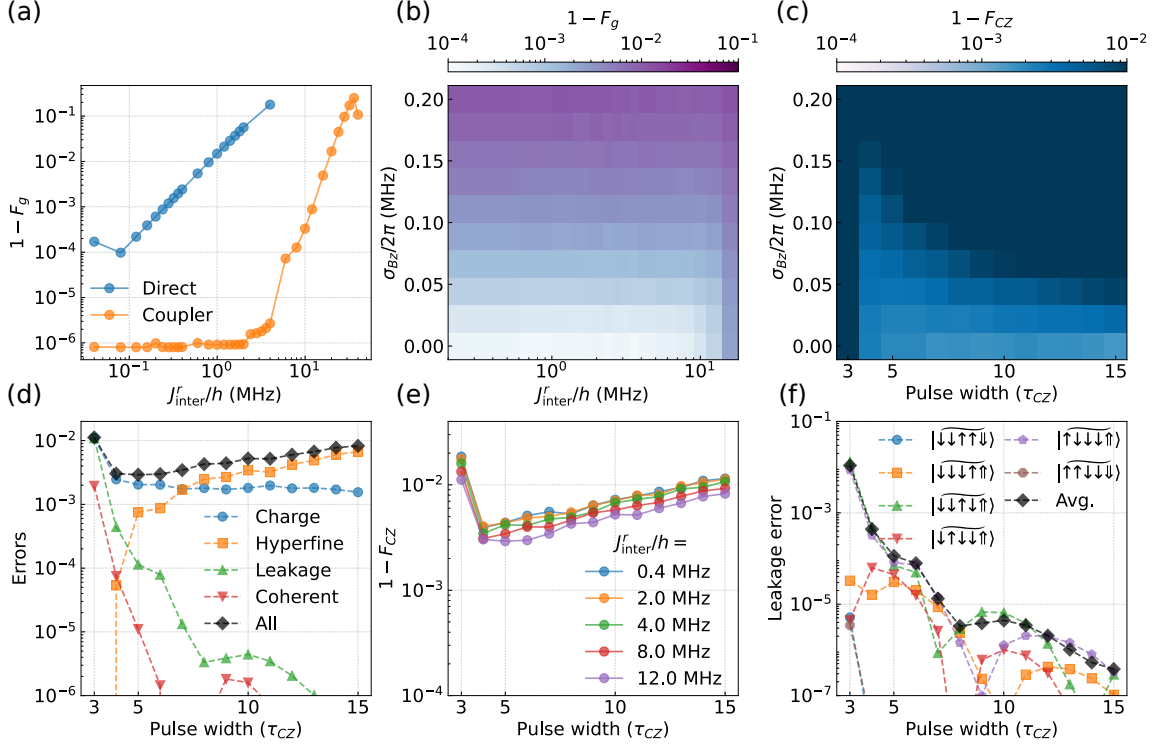


FIG. 7. $X_{\pi/2}$ and CZ gate error of two RST qubits coupled by a single-spin coupler. (a) A comparison of the coherent error of the $X_{\pi/2}$ gate against inter-qubit residual exchange between two RST qubits with direct and coupler-assisted coupling. The inter-qubit coupling for the coupler case refers to the coupler-spin couplings $J_{2c}^r = J_{3c}^r = J_{inter}^r$. Both cases use a gate time of $15\tau_L$, which is also used in (b). $J_{inter}^r/h = 12$ MHz are used in (c), (d), and (f). (b) $X_{\pi/2}$ gate error with varying J_{inter}^r under different hyperfine noise strengths σ_{Bz}^z . Charge noise contributions are included. (c) CZ gate error with varying CZ gate pulse width and hyperfine noise strength. Charge noise contributions are included. (d) Error budget of the CZ gate with hyperfine noise strength $\sigma_{Bz} = 2\pi \times 0.04$ MHz. (e) CZ gate error with varying CZ gate pulse width and inter-qubit residual exchange coupling. Both noise types are applied at the same level as (d). (f) Leakage error of a coupler-assisted CZ gate with varying CZ gate pulse width.

the average energy spacing between each of the coupled computational-leakage state pairs:

$$\tau_{CZ}^{-1} = \frac{1}{4h} \left(|\Delta E_{\uparrow\downarrow\uparrow\downarrow,11}| + |\Delta E_{\downarrow\downarrow\uparrow\uparrow,00}| + |\Delta E_{\downarrow\uparrow\downarrow\uparrow,10}| + |\Delta E_{\downarrow\uparrow\downarrow\uparrow,10}| \right), \quad (33)$$

where $\Delta E_{kl} = E_k - E_l$ is the energy difference between states $|k\rangle$ and $|l\rangle$. As the coupler frequency is fixed at $\Delta_{23,c} = 0$ and the system is configured with the parameters listed in Table I, we calculate $\tau_{CZ} \approx 16.50$ ns.

For hyperfine noise levels lower than $2\pi \times 0.50$ MHz, charge noise becomes dominant error source and contributes an error background of about 2×10^{-3} . As above, the non-monotonic dependence of the CZ gate error on the pulse width occurs due to the tradeoff between leakage and hyperfine errors. The error budget with a fixed hyperfine noise amplitude $\sigma_{Bz} = 2\pi \times 0.04$ MHz is shown in Fig. 7(d), where the optimum configuration is at about $4\tau_{CZ} \approx 66$ ns, corresponding to a CZ gate error of 3×10^{-3} . Since the coupler-assisted CZ gate requires a higher-amplitude inter-qubit exchange pulse compared

to the directly-coupled case, an overall increase in the charge noise contribution is observed compared to the directly-coupled case. Fig. 7(e) shows the CZ gate error with different pulse widths and inter-qubit residual exchange values in the presence of both hyperfine and charge noise at the same level of Fig. 7(d). We observe a small dependence of the error on J_{inter}^r due to the small variations of charge noise sensitivities.

The primary source of leakage arises from coupler excitations due to the low adiabaticity of the exchange pulse envelope. By shaping the envelope as a cosine function without a flat plateau, the total leakage error can be suppressed below 10^{-4} . Fig. 7(f) shows the leakage error during a CZ gate. At the trade-off point of $4\tau_{CZ}$, the leakage error is approximately 4×10^{-4} —significantly lower than the contributions from both charge and hyperfine noise.

As mentioned earlier, this analysis assumes perfect initialization of the coupler, for which an optimal error rate of 2.6×10^{-3} has been realistically demonstrated for single-spin initialization [81]. Any residual coupler excitation will result in a leakage error, which is a chal-

lenge also encountered in superconducting qubits with tunable couplers [82, 83]. Fast and high-fidelity coupler initialization protocols are therefore essential for scalable operation of spin-coupler architectures. One promising approach involves quantum non-demolition (QND) measurement of the coupler spin, where the expected outcome is spin-down [84]. If the QND measurement yields spin-up, the initialized state can be discarded—effectively implementing a mechanism similar to erasure encoding [85].

V. CONCLUSION AND OUTLOOK

In conclusion, we analyzed single- and two-qubit control errors resulting from both inter- and intra-qubit residual exchange coupling in systems of exchange-coupled RST qubits. We showed that commensurate driving can mitigate coherent and leakage errors in both single- and two-qubit gates. For intra-qubit residual exchange values below a few hundred kHz, gate fidelities are limited by the interplay of hyperfine and charge noise. For residual exchange values above this level, single-qubit gates suffer from a quantum crosstalk error. We showed that a single-spin coupler between RST qubits can suppress this error by two orders of magnitude. The large on-off ratio that can be achieved with the coupler suggests that a fast CPhase gate with minimal coherent and leakage error can be achieved. The RST-coupler-RST architecture offers a pathway to constructing crosstalk-free unit cells for large-scale semiconductor quantum dot arrays.

VI. DATA AVAILABILITY

The data and simulation scripts are available at <https://doi.org/10.5281/zenodo.17794872> [86].

VII. ACKNOWLEDGMENTS

J.D. acknowledges discussions with Pan Shi, Meng Wang, and Feiyang Ye. This work was sponsored by the Army Research Office through Grant No. W911NF-23-1-0115 and the Air Force Office of Scientific Research through Grant No. FA9550-23-1-0710. The views and conclusions contained in this document are those of the authors and should not be interpreted as representing the official policies, either expressed or implied, of the Army Research Office or the U.S. Government. The U.S. Government is authorized to reproduce and distribute reprints for Government purposes notwithstanding any copyright notation herein.

Appendix A: Driving a RST qubit

In this section we will derive the single-RST-qubit Hamiltonian under a resonant intra-qubit exchange drive with the rotating wave approximation. Considering a Heisenberg model for two spins with corresponding Zeeman terms, the total Hamiltonian is given by

$$H_s = -\frac{1}{2}\hbar\omega_{s1}s_1^z - \frac{1}{2}\hbar\omega_{s2}s_2^z + \frac{1}{4}J_{12}^r\vec{s}_1 \cdot \vec{s}_2, \quad (\text{A1})$$

where \hbar is the reduced Planck constant, J_{12}^r is the residual exchange between spins S_1 and S_2 , s_k^μ with $\mu \in \{x, y, z\}$ and $k = 1, 2$ are the Pauli operators for spin k . The Pauli-vector $\vec{s}_k = (s_k^x, s_k^y, s_k^z)$, and the Larmor frequency for spin k is defined as $\hbar\omega_{s,k} = g_k\mu_B B_k^z$.

We construct the encoded Pauli operators in the two-spin decoherence-free subspace (DFS₂) as

$$\bar{\sigma}_x = \frac{1}{2}(s_1^x s_2^x + s_1^y s_2^y), \quad (\text{A2})$$

$$\bar{\sigma}_y = \frac{1}{2}(s_1^y s_2^x - s_1^x s_2^y), \quad (\text{A3})$$

$$\bar{\sigma}_z = -\frac{i}{2}[\bar{\sigma}_x, \bar{\sigma}_y]. \quad (\text{A4})$$

By ignoring a global phase depending on J_{12}^r , the Hamiltonian within the DFS₂ is given by

$$\bar{H}_0 = -\frac{1}{2}\hbar\bar{\omega}\bar{\sigma}_z + \frac{1}{2}J_{12}^r\bar{\sigma}_x, \quad (\text{A5})$$

where $\bar{\omega} = |\omega_{s1} - \omega_{s2}|$. After diagonalization, the RST qubit static Hamiltonian becomes

$$H_0 = -\frac{1}{2}\hbar\omega_q\sigma_z, \quad (\text{A6})$$

where $\omega_q = \sqrt{\bar{\omega}^2 + (J_{12}^r/\hbar)^2}$, and σ_μ , $\mu \in \{x, y, z\}$, are the Pauli operators of the RST qubits. The unitary transformation between basis σ_k and $\bar{\sigma}_k$ is a rotation operator along the y -axis

$$\bar{R}_y(\Theta) = \exp\left(-i\frac{\Theta}{2}\bar{\sigma}_y\right), \quad (\text{A7})$$

where $\cos\Theta = \bar{\omega}/\omega_q$, and $\sin\Theta = J_{12}^r/(\hbar\omega_q)$. When an intra-qubit exchange drive $J_{12}(t)$ is applied, the time-dependent Hamiltonian can be formulated into static [Eq. (A5)] and driven parts, given by

$$\begin{aligned} \bar{H}(t) &= -\frac{1}{2}\hbar\bar{\omega}\bar{\sigma}_z + J_{12}(t)\bar{\sigma}_x \\ &= \bar{H}_0 + \bar{H}_d(t). \end{aligned} \quad (\text{A8})$$

with

$$\bar{H}_d(t) = \frac{1}{2}[J_{12}(t) - J_{12}^r]\bar{\sigma}_x. \quad (\text{A9})$$

Note that while $J_{12}(t)$ contains J_{12}^r , the driven part contains only the time-dependent exchange coupling.

Moving into the qubit eigenbasis by applying the unitary transformation in Eq. (A7), the Hamiltonian $H(t) = \bar{R}_y(\Theta) \bar{H}(t) \bar{R}_y^\dagger(\Theta)$ becomes

$$H(t) = H_0 + H_d(t), \quad (\text{A10})$$

$$H_d(t) = \frac{1}{2} [J_{12}(t) - J_{12}^r] (\cos \Theta \sigma_x - \sin \Theta \sigma_z). \quad (\text{A11})$$

The exchange driven single-qubit rotations have both x and z components, due to the non-zero intra-qubit residual exchange coupling. By taking the drive as in Eq. (10), the effective Hamiltonian in the rotating frame with respect to the driving frequency becomes

$$H_{\text{eff}}(t) = i\hbar \dot{U}_{\text{rt}} U_{\text{rt}}^\dagger + U_{\text{rt}} H U_{\text{rt}}^\dagger = \tilde{H}_0 + \tilde{H}_d(t), \quad (\text{A12})$$

where $U_{\text{rt}} = \exp(-i\omega_d t \sigma_z / 2)$. The static and driving terms in the rotating frame are given by

$$\tilde{H}_0 = -\frac{1}{2} \hbar \delta_q \sigma_z, \quad (\text{A13})$$

$$\begin{aligned} \tilde{H}_d(t) &= \frac{1}{2} [J_{12}(t) - J_{12}^r] \\ &\times \left(\cos \Theta U_{\text{rt}} \sigma_x U_{\text{rt}}^\dagger - \sin \Theta U_{\text{rt}} \sigma_z U_{\text{rt}}^\dagger \right), \end{aligned} \quad (\text{A14})$$

where $\delta_q = |\omega_q - \omega_d|$. The transformed Pauli operators are given by

$$U_{\text{rt}} \sigma_x U_{\text{rt}}^\dagger = \begin{bmatrix} 0 & e^{-i\omega_d t} \\ e^{i\omega_d t} & 0 \end{bmatrix}, \quad (\text{A15})$$

$$U_{\text{rt}} \sigma_z U_{\text{rt}}^\dagger = \sigma_z. \quad (\text{A16})$$

When the drive frequency is resonant with the qubit frequency, i.e., $\delta_q = 0$, the effective Hamiltonian in the rotating frame reduces to Eq. (12).

Appendix B: Direct coupling

In this section, we will calculate the ZZ-interaction from residual inter-qubit exchange coupling. Consider a one-dimensional spin chain with spins at each site labeled as S_k , where $k \in 1, 2, 3, 4$. The Hamiltonian is

$$H_s = -\frac{1}{2} \sum_{k=1}^4 \hbar \omega_{s,k} s_k^z + \frac{1}{4} \sum_{k=1}^3 J_{k,k+1}^r \vec{s}_k \cdot \vec{s}_{k+1}, \quad (\text{B1})$$

where $\hbar \omega_{s,k}$ is the Zeeman energy of spin k , and $J_{k,k+1}^r$ is the residual exchange coupling between spin k and $k+1$. For small residual exchange coupling ($J_{k,k+1}^r \ll \hbar |\omega_{s,k} - \omega_{s,k+1}|$), the Heisenberg part can be treated as a perturbation. The perturbative expansion of the eigenenergies up to second-order is given by

$$E_n = E_n^{(0)} + \sum_k \frac{J_{k,k+1}^r}{4} E_{n,k}^{(1)} + \sum_{k,l} \frac{J_{k,k+1}^r J_{l,l+1}^r}{16} E_{n,kl}^{(2)}, \quad (\text{B2})$$

where the correction at each order is calculated as

$$E_{n,k}^{(1)} = \langle n^{(0)} | \vec{s}_k \cdot \vec{s}_{k+1} | n^{(0)} \rangle, \quad (\text{B3})$$

$$E_{n,kl}^{(2)} = \sum_{m \neq n} \frac{\langle n^{(0)} | \vec{s}_k \cdot \vec{s}_{k+1} | m^{(0)} \rangle \langle m^{(0)} | \vec{s}_l \cdot \vec{s}_{l+1} | n^{(0)} \rangle}{E_n^{(0)} - E_m^{(0)}}. \quad (\text{B4})$$

Here $|n^{(0)}\rangle \in \mathcal{C}$ is the unperturbed eigenstates inside the computational subspace \mathcal{C} , $|m^{(0)}\rangle \in \mathcal{M}$ is unperturbed eigenstates inside the two-excitation manifold \mathcal{M} , and $k, l \in \{1, 2, 3\}$. The set of unperturbed eigenstates with two excitations is $\mathcal{M} = \mathcal{C} \cup \mathcal{L}$, where the basis states for the computational and leakage subspaces are $\mathcal{C} = \{|\downarrow\uparrow\downarrow\uparrow\rangle, |\downarrow\uparrow\uparrow\downarrow\rangle, |\uparrow\downarrow\downarrow\uparrow\rangle, |\uparrow\downarrow\uparrow\downarrow\rangle\}$, and $\mathcal{L} = \{|\uparrow\uparrow\downarrow\downarrow\rangle, |\downarrow\downarrow\uparrow\uparrow\rangle\}$, respectively. The static ZZ-interaction is defined as

$$\zeta = E_{\uparrow\downarrow\uparrow\downarrow} + E_{\downarrow\uparrow\uparrow\downarrow} - E_{\uparrow\downarrow\downarrow\uparrow} - E_{\downarrow\uparrow\uparrow\downarrow}, \quad (\text{B5})$$

which is identical to Eq. (2). The only non-zero contribution from the perturbative expansion is the first-order correction

$$\begin{aligned} \zeta^{(1)} &= \frac{1}{4} \sum_{k=1}^3 J_{k,k+1}^r \left(E_{\uparrow\downarrow\uparrow\downarrow,k}^{(1)} + E_{\downarrow\uparrow\uparrow\downarrow,k}^{(1)} \right. \\ &\quad \left. - E_{\uparrow\downarrow\downarrow\uparrow,k}^{(1)} - E_{\downarrow\uparrow\uparrow\downarrow,k}^{(1)} \right) \\ &= -J_{23}^r. \end{aligned} \quad (\text{B6})$$

Therefore, the residual ZZ-interaction is given by the first-order contribution $\zeta^{(1)}$

$$\zeta = -J_{23}^r. \quad (\text{B7})$$

Appendix C: Spin coupler

In this section we calculate the ZZ-interaction mediated by a single-spin coupler between two RST qubits. Consider a one-dimensional Heisenberg model for five spins with Hamiltonian

$$\begin{aligned} H_{\text{sc}} &= -\frac{1}{2} \sum_{k=1}^4 \hbar \omega_{s,k} s_k^z + \frac{1}{4} \sum_{k=1,3} J_{k,k+1}^r \vec{s}_k \cdot \vec{s}_{k+1} \\ &\quad - \frac{1}{2} \hbar \omega_{sc} s_c^z + \frac{1}{4} \sum_{k=2,3} J_{k,c}^r \vec{s}_k \cdot \vec{s}_c, \end{aligned} \quad (\text{C1})$$

where $\hbar \omega_{s,k} = g_k \mu_B B_c^z$ is the Zeeman energy of spin $k \in \{1, 2, 3, 4, c\}$, J_{12}^r and J_{34}^r intra-qubit residual exchange couplings, J_{2c}^r and J_{3c}^r are inter-qubit residual exchange couplings. Treating all diagonal terms (s_k^z and $s_k^z s_l^z$) as static H_0 and all x and y terms as perturbations, we define

$$V = \frac{1}{2} \sum_{k=1,3} J_{k,k+1}^r V_{k,k+1} + \frac{1}{2} \sum_{l=2,3} J_{l,c}^r V_{l,c}, \quad (\text{C2})$$

where $V_{k,k+1} = s_k^+ s_{k+1}^- + s_k^- s_{k+1}^+$, and $V_{k,c} = s_k^+ s_c^- + s_k^- s_c^+$ for $k \in \{1, 3\}$ and $l \in \{2, 3\}$, respectively.

Using labels $|S_1 S_2 S_3 S_4 S_c\rangle$ to denote states, the basis states for the unperturbed computational and leakage states are $\mathcal{C} = \{|\downarrow\uparrow\downarrow\downarrow\rangle, |\downarrow\uparrow\uparrow\downarrow\rangle, |\uparrow\uparrow\downarrow\downarrow\rangle, |\uparrow\downarrow\uparrow\downarrow\rangle\}$, and $\mathcal{L} = \{|\uparrow\downarrow\downarrow\uparrow\rangle, |\downarrow\downarrow\downarrow\uparrow\rangle, |\downarrow\downarrow\uparrow\uparrow\rangle, |\downarrow\downarrow\uparrow\downarrow\rangle, |\uparrow\uparrow\downarrow\downarrow\rangle\}$. For clarity, we use the double arrow to represent the coupler spin.

The ZZ-interaction is given by

$$\zeta = E_{\uparrow\downarrow\uparrow\downarrow} + E_{\downarrow\uparrow\uparrow\downarrow} - E_{\uparrow\downarrow\uparrow\downarrow} - E_{\downarrow\uparrow\uparrow\downarrow}. \quad (\text{C3})$$

The terms giving non-zero contribution to this ZZ-interaction appear at second-order

$$\zeta^{(2)} = E_{\uparrow\downarrow\uparrow\downarrow}^{(2)} + E_{\downarrow\uparrow\uparrow\downarrow}^{(2)} - E_{\uparrow\downarrow\uparrow\downarrow}^{(2)} - E_{\downarrow\uparrow\uparrow\downarrow}^{(2)}, \quad (\text{C4})$$

where the second-order energy correction is calculated by

$$E_n^{(2)} = \sum_{m \neq n} \frac{\langle n^{(0)} | V | m^{(0)} \rangle \langle m^{(0)} | V | n^{(0)} \rangle}{E_n^{(0)} - E_m^{(0)}}. \quad (\text{C5})$$

Here $|n^{(0)}\rangle \in \mathcal{C}$ and $|m^{(0)}\rangle \in \mathcal{C} \cup \mathcal{L}$ are the unperturbed eigenstates, and $E_n^{(0)}$ is the unperturbed eigenenergy. The final result shows

$$\begin{aligned} \zeta^{(2)} = & \frac{(J_{2c}^r)^2}{2} \left(\frac{1}{2\hbar\Delta_{2c} + J_{3c}^r - J_{12}^r} \right. \\ & \left. - \frac{1}{2\hbar\Delta_{2c} - J_{3c}^r - J_{12}^r} \right) \\ & + \frac{(J_{3c}^r)^2}{2} \left(\frac{1}{2\hbar\Delta_{3c} + J_{2c}^r - J_{34}^r} \right. \\ & \left. - \frac{1}{2\hbar\Delta_{3c} - J_{2c}^r - J_{34}^r} \right), \end{aligned} \quad (\text{C6})$$

where $\Delta_{kl} = \omega_{s,k} - \omega_{s,l}$ for $k, l \in \{1, 2, 3, 4, c\}$. When the nearest-neighbor detuning is large, i.e. when $2\hbar\Delta_{2c} \gg J_{3c}^r \pm J_{12}^r$ and $2\hbar\Delta_{3c} \gg J_{3c}^r \pm J_{12}^r$, the ZZ-interaction can be expanded to

$$\zeta \approx -\frac{J_{2c}^r J_{3c}^r}{4\hbar^2} \left(\frac{J_{2c}^r}{\Delta_{2c}^2} + \frac{J_{3c}^r}{\Delta_{3c}^2} \right). \quad (\text{C7})$$

Appendix D: Charge noise

We simulate the effect of charge and hyperfine noise using a Monte Carlo approach. We generate a simulated charge noise time series $\delta V[n]$ using the method mentioned in Refs. [74, 87]. For a simulated evolution from time 0 to T taking N points, a zero mean and unit variance Gaussian white noise time series $u[n] \sim \mathcal{N}(0, 1)$ with length N is generated. The Fourier transform of $u[n]$ is computed as $\tilde{u}[n] = \mathcal{F}\{u\}[n]$. For a noise time series $\delta V[n]$ with $1/f^\beta$ power spectrum density (PSD)

$$S_{V_B}(f) = \frac{A_\mu^2 / \gamma^2}{f^\beta}, \quad (\text{D1})$$

its Fourier component $\delta\tilde{V}[n]$ can be computed as

$$\delta\tilde{V}[n] = \frac{A_\mu}{\gamma} \sqrt{\frac{N}{T}} \left(\frac{n-1}{T} \right)^{-\beta} \tilde{u}[n], \quad (\text{D2})$$

where A_μ is the amplitude of the power spectral density at one Hertz, and $\gamma = 0.1$ eV/V is the lever arm. The time series of the noise is obtained by the inverse Fourier transform of the Fourier coefficients:

$$\delta V[n] = \mathcal{F}^{-1}\{\delta\tilde{V}\}[n]. \quad (\text{D3})$$

In the n -th point during a single-run of the simulation, the applied barrier voltage at this point is given by $V_B[n] + \delta V[n]$. Here, $V_B[n]$ is the barrier gate voltage resulting a desired exchange coupling $J[n]$ at point n of during exchange drive $J(t)$. Using the empirical relation between exchange coupling and barrier voltage in Eq. (4), the noisy exchange coupling series can be calculated through

$$J[n] = J^r e^{2\alpha(V_B[n] + \delta V[n])}, \quad (\text{D4})$$

where J^r is the residual exchange coupling, and α is the barrier-exchange lever arm. During each run of the simulation, the charge noise series is regenerated based on this method.

Appendix E: Hyperfine noise

A quasistatic white hyperfine noise is applied on individual spins. For a single spin in isotopically purified ^{28}Si , the coherence time limited by hyperfine noise is above $5 \mu\text{s}$ [5, 19, 24]. The coherence time limited by the hyperfine noise amplitude in the simulation is calibrated by a simulated Ramsey sequence as shown in Fig. 8(a). The simulated T_2^* at different values σ_{Bz} is fitted by a quasistatic noise model:

$$T_2^*(\sigma_{Bz}) = \frac{\Omega}{\sigma_{Bz}}, \quad (\text{E1})$$

where the fitted result is shown Fig. 8(b) with $\Omega = 0.112$. We extract the T_2^* by fitting the simulated data (spin-down population P_\downarrow vs hold time t) with a Gaussian decay envelope

$$P_\downarrow(t) = A e^{-(t/T_2^*)^2} \cos(2\pi f t + \phi) + B. \quad (\text{E2})$$

Fig. 8(c) show a simulated Ramsey experiment with $\sigma_{Bz} = 2\pi \times 0.04$ MHz, where the fitted $T_2^* = 2.81 \mu\text{s}$.

Appendix F: Gate fidelity

The averaged gate fidelity F_g [88–90] is used to evaluate both single- and two-qubit gate fidelities in our system. A straightforward approach to calculate the average gate fidelity of a noisy process $U(\tau)$ from time 0 to

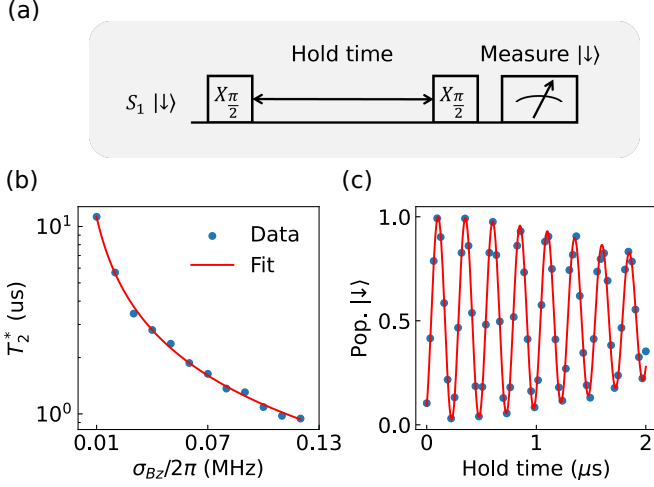


FIG. 8. Simulating a single-spin (Loss-Divincenzo) qubit coherence time under varying hyperfine noise levels. (a) Ramsey sequence for measuring T_2^* . (b) Extracted T_2^* fitted with the quasistatic model. (c) Ramsey data with hyperfine noise level $\sigma_{Bz} = 2\pi \times 0.04\text{MHz}$ with fitted $T_2^* = 2.81\mu\text{s}$.

τ compared to a noiseless ideal process U_{ideal} is from its entanglement fidelity, given by

$$F_e = \frac{1}{4^d} \sum_{\rho \in \{\rho_0\}} \text{Tr}[\rho_\tau(\rho) \rho_{\text{ideal}}(\rho)]. \quad (\text{F1})$$

Here, $\{\rho_0\}$ is a complete set of fiducial states in a n -qubit Herbert space, $\rho_\tau(\rho) = U(\tau)\rho U^\dagger(\tau)$, and $\rho_{\text{ideal}}(\rho) = U_{\text{ideal}}\rho U_{\text{ideal}}^\dagger$. The relation between the average gate fidelity F_g and entanglement fidelity F_e under

this n -qubit Herbert space is given by [91, 92]

$$F_g = \frac{2^n F_e + 1}{2^n + 1}. \quad (\text{F2})$$

For single-qubit $n = 1$ case, the complete set of fiducial states is given by

$$\{\rho_0\} = \left\{ |0\rangle, |1\rangle, \frac{1}{\sqrt{2}}(|0\rangle + |1\rangle), \frac{1}{\sqrt{2}}(|0\rangle + i|1\rangle) \right\}. \quad (\text{F3})$$

Inside the single-RST-qubit computational subspace $\{|0\rangle, |1\rangle\} = \{|\downarrow\uparrow\rangle, |\uparrow\downarrow\rangle\}$, Eq.(F3) becomes exactly the set of initial states in Eq.(26). The single-qubit entanglement F_e and averaged gate fidelity F_g are given by

$$F_e = \frac{1}{4} \sum_{\rho \in \{\rho_0\}} \text{Tr}[\rho_\tau(\rho) \rho_{\text{ideal}}(\rho)], \quad (\text{F4})$$

$$F_g = \frac{1}{3} (2F_e + 1). \quad (\text{F5})$$

For the two qubit $n = 2$ case, the complete set of fiducial states is given by

$$\{\rho'_0\} = \{\rho_A \otimes \rho_B | \rho_A, \rho_B \in \{\rho_0\}\}. \quad (\text{F6})$$

For the two-qubit CZ gate, its entanglement F_{CZ}^e and averaged gate fidelity F_{CZ} are given by

$$F_{CZ}^e = \frac{1}{16} \sum_{\rho \in \{\rho'_0\}} \text{Tr}[\rho_\tau(\rho) \rho_{\text{ideal}}(\rho)], \quad (\text{F7})$$

$$F_{CZ} = \frac{1}{5} (4F_{CZ}^e + 1), \quad (\text{F8})$$

where $U_{\text{ideal}} = \text{diag}(1, 1, 1, -1)$.

-
- [1] G. Burkard, T. D. Ladd, A. Pan, J. M. Nichol, and J. R. Petta, Semiconductor spin qubits, *Reviews of Modern Physics* **95**, 025003 (2023).
- [2] K. Takeda, A. Noiri, T. Nakajima, T. Kobayashi, and S. Tarucha, Quantum error correction with silicon spin qubits, *Nature* **608**, 682 (2022).
- [3] F. Van Riggelen, W. Lawrie, M. Russ, N. Hendrickx, A. Sammak, M. Rispler, B. Terhal, G. Scappucci, and M. Veldhorst, Phase flip code with semiconductor spin qubits, *npj Quantum information* **8**, 124 (2022).
- [4] B. Hetényi and J. R. Wootton, Tailoring quantum error correction to spin qubits, *Physical Review A* **109**, 032433 (2024).
- [5] P. Steinacker, N. Dumoulin Stuyck, W. H. Lim, T. Tanttu, M. Feng, S. Serrano, A. Nickl, M. Candido, J. D. Cifuentes, E. Vahapoglu, *et al.*, Industry-compatible silicon spin-qubit unit cells exceeding 99% fidelity, *Nature*, 1 (2025).
- [6] T. F. Watson, B. Weber, Y.-L. Hsueh, L. C. Hollenberg, R. Rahman, and M. Y. Simmons, Atomically engineered electron spin lifetimes of 30 s in silicon, *Science advances* **3**, e1602811 (2017).
- [7] C. Yang, A. Rossi, R. Ruskov, N. Lai, F. Mohiyaddin, S. Lee, C. Tahan, G. Klimeck, A. Morello, and A. Dzurak, Spin-valley lifetimes in a silicon quantum dot with tunable valley splitting, *Nature communications* **4**, 2069 (2013).
- [8] P. Stano and D. Loss, Review of performance metrics of spin qubits in gated semiconducting nanostructures, *Nature Reviews Physics* **4**, 672 (2022).
- [9] N. D. Foster, J. D. Henshaw, M. Rudolph, D. R. Luhman, and R. M. Jock, Dephasing and error dynamics affecting a singlet-triplet qubit during coherent spin shuttling, *npj Quantum Information* **11**, 63 (2025).
- [10] M. De Smet, Y. Matsumoto, A.-M. J. Zwerver, L. Trypuzen, S. L. de Snoo, S. V. Amitonov, S. R. Katirae-Far, A. Sammak, N. Samkharadze, Ö. Gül, *et al.*, High-fidelity single-spin shuttling in silicon, *Nature Nanotechnology*, 1 (2025).
- [11] R. Xue, M. Beer, I. Seidler, S. Humpohl, J.-S. Tu, S. Trelenkamp, T. Struck, H. Bluhm, and L. R. Schreiber, Si/sige qubus for single electron information-processing devices with memory and micron-scale connectivity function, *Nature Communications* **15**, 2296 (2024).

- [12] F. van Riggelen-Doelman, C.-A. Wang, S. L. de Snoo, W. I. Lawrie, N. W. Hendrickx, M. Rimbach-Russ, A. Sammak, G. Scappucci, C. Déprez, and M. Veldhorst, Coherent spin qubit shuttling through germanium quantum dots, *Nature Communications* **15**, 5716 (2024).
- [13] A. Noiri, K. Takeda, T. Nakajima, T. Kobayashi, A. Sammak, G. Scappucci, and S. Tarucha, A shuttling-based two-qubit logic gate for linking distant silicon quantum processors, *nature communications* **13**, 5740 (2022).
- [14] B. Jadot, P.-A. Mortemousque, E. Chanrion, V. Thiney, A. Ludwig, A. D. Wieck, M. Urdampilleta, C. Bäuerle, and T. Meunier, Distant spin entanglement via fast and coherent electron shuttling, *Nature Nanotechnology* **16**, 570 (2021).
- [15] A. Mills, D. Zajac, M. Gullans, F. Schupp, T. Hazard, and J. R. Petta, Shuttling a single charge across a one-dimensional array of silicon quantum dots, *Nature communications* **10**, 1063 (2019).
- [16] S. D. Ha, E. Acuna, K. Raach, Z. T. Bloom, T. L. Brecht, J. M. Chappell, M. D. Choi, J. E. Christensen, I. T. Counts, D. Daprano, *et al.*, Two-dimensional si spin qubit arrays with multilevel interconnects, *PRX Quantum* **6**, 030327 (2025).
- [17] A. J. Weinstein, M. D. Reed, A. M. Jones, R. W. Andrews, D. Barnes, J. Z. Blumoff, L. E. Euliss, K. Eng, B. H. Fong, S. D. Ha, *et al.*, Universal logic with encoded spin qubits in silicon, *Nature* **615**, 817 (2023).
- [18] L. M. Vandersypen, H. Bluhm, J. S. Clarke, A. S. Dzurak, R. Ishihara, A. Morello, D. J. Reilly, L. R. Schreiber, and M. Veldhorst, Interfacing spin qubits in quantum dots and donors—hot, dense, and coherent, *npj Quantum Information* **3**, 34 (2017).
- [19] S. Neyens, O. K. Zietz, T. F. Watson, F. Luthi, A. Nethewala, H. C. George, E. Henry, M. Islam, A. J. Wagner, F. Borjans, *et al.*, Probing single electrons across 300-mm spin qubit wafers, *Nature* **629**, 80 (2024).
- [20] A. Zwerver, T. Krähenmann, T. Watson, L. Lampert, H. C. George, R. Pillarisetty, S. Bojarski, P. Amin, S. Amitonov, J. Boter, *et al.*, Qubits made by advanced semiconductor manufacturing, *Nature Electronics* **5**, 184 (2022).
- [21] A. S. Rao, D. Buterakos, B. van Straaten, V. John, C. X. Yu, S. D. Oosterhout, L. Stehouwer, G. Scappucci, M. Veldhorst, F. Borsoi, *et al.*, Modular autonomous virtualization system for two-dimensional semiconductor quantum dot arrays, *Physical Review X* **15**, 021034 (2025).
- [22] F. Borsoi, N. W. Hendrickx, V. John, M. Meyer, S. Motz, F. Van Riggelen, A. Sammak, S. L. De Snoo, G. Scappucci, and M. Veldhorst, Shared control of a 16 semiconductor quantum dot crossbar array, *Nature Nanotechnology* **19**, 21 (2024).
- [23] V. John, C. X. Yu, B. van Straaten, E. A. Rodríguez-Mena, M. Rodríguez, S. Oosterhout, L. E. Stehouwer, G. Scappucci, S. Bosco, M. Rimbach-Russ, *et al.*, A two-dimensional 10-qubit array in germanium with robust and localised qubit control, *arXiv preprint arXiv:2412.16044* (2024).
- [24] X. Xue, M. Russ, N. Samkharadze, B. Undseth, A. Sammak, G. Scappucci, and L. M. Vandersypen, Quantum logic with spin qubits crossing the surface code threshold, *Nature* **601**, 343 (2022).
- [25] A. Noiri, K. Takeda, T. Nakajima, T. Kobayashi, A. Sammak, G. Scappucci, and S. Tarucha, Fast universal quantum gate above the fault-tolerance threshold in silicon, *Nature* **601**, 338 (2022).
- [26] A. R. Mills, C. R. Guinn, M. J. Gullans, A. J. Sigillito, M. M. Feldman, E. Nielsen, and J. R. Petta, Two-qubit silicon quantum processor with operation fidelity exceeding 99%, *Science Advances* **8**, eabn5130 (2022).
- [27] A. G. Fowler, M. Mariantoni, J. M. Martinis, and A. N. Cleland, Surface codes: Towards practical large-scale quantum computation, *Physical Review A—Atomic, Molecular, and Optical Physics* **86**, 032324 (2012).
- [28] J. P. Bonilla Ataides, D. K. Tuckett, S. D. Bartlett, S. T. Flammia, and B. J. Brown, The xzxx surface code, *Nature communications* **12**, 2172 (2021).
- [29] J. R. Petta, A. C. Johnson, J. M. Taylor, E. A. Laird, A. Yacoby, M. D. Lukin, C. M. Marcus, M. P. Hanson, and A. C. Gossard, Coherent manipulation of coupled electron spins in semiconductor quantum dots, *Science* **309**, 2180 (2005).
- [30] E. A. Laird, J. M. Taylor, D. P. DiVincenzo, C. M. Marcus, M. P. Hanson, and A. C. Gossard, Coherent spin manipulation in an exchange-only qubit, *Physical Review B—Condensed Matter and Materials Physics* **82**, 075403 (2010).
- [31] D. Kim, Z. Shi, C. Simmons, D. Ward, J. Prance, T. S. Koh, J. K. Gamble, D. Savage, M. Lagally, M. Friesen, *et al.*, Quantum control and process tomography of a semiconductor quantum dot hybrid qubit, *Nature* **511**, 70 (2014).
- [32] K. Eng, T. D. Ladd, A. Smith, M. G. Borselli, A. A. Kiselev, B. H. Fong, K. S. Holabird, T. M. Hazard, B. Huang, P. W. Deelman, *et al.*, Isotopically enhanced triple-quantum-dot qubit, *Science advances* **1**, e1500214 (2015).
- [33] J. Z. Blumoff, A. S. Pan, T. E. Keating, R. W. Andrews, D. W. Barnes, T. L. Brecht, E. T. Croke, L. E. Euliss, J. A. Fast, C. A. Jackson, *et al.*, Fast and high-fidelity state preparation and measurement in triple-quantum-dot spin qubits, *PRX Quantum* **3**, 010352 (2022).
- [34] C. Barthel, D. Reilly, C. M. Marcus, M. Hanson, and A. Gossard, Rapid single-shot measurement of a singlet-triplet qubit, *Physical Review Letters* **103**, 160503 (2009).
- [35] T. Nakajima, M. R. Delbecq, T. Otsuka, P. Stano, S. Amaha, J. Yoneda, A. Noiri, K. Kawasaki, K. Takeda, G. Allison, *et al.*, Robust single-shot spin measurement with 99.5% fidelity in a quantum dot array, *Physical review letters* **119**, 017701 (2017).
- [36] P. Harvey-Collard, B. D’Anjou, M. Rudolph, N. T. Jacobson, J. Dominguez, G. A. Ten Eyck, J. R. Wendt, T. Pluym, M. P. Lilly, W. A. Coish, *et al.*, High-fidelity single-shot readout for a spin qubit via an enhanced latching mechanism, *Physical Review X* **8**, 021046 (2018).
- [37] K. Takeda, A. Noiri, T. Nakajima, L. C. Camenzind, T. Kobayashi, A. Sammak, G. Scappucci, and S. Tarucha, Rapid single-shot parity spin readout in a silicon double quantum dot with fidelity exceeding 99%, *npj Quantum Information* **10**, 22 (2024).
- [38] S. Park, J. Benson, J. Corrigan, J. Dodson, S. Copper-smith, M. Friesen, and M. Eriksson, Single shot latched readout of a quantum dot qubit using barrier gate pulsing, *npj Quantum Information* **11**, 148 (2025).
- [39] B. Sun, T. Brecht, B. H. Fong, M. Akmal, J. Z. Blumoff, T. A. Cain, F. W. Carter, D. H. Finestone, M. N. Fireman, W. Ha, *et al.*, Full-permutation dynamical decou-

- pling in triple-quantum-dot spin qubits, *PRX Quantum* **5**, 020356 (2024).
- [40] H. Bluhm, S. Foletti, I. Neder, M. Rudner, D. Mahalu, V. Umansky, and A. Yacoby, Dephasing time of gaa electron-spin qubits coupled to a nuclear bath exceeding 200 μ s, *Nature Physics* **7**, 109 (2011).
- [41] M. Friesen, J. Ghosh, M. Eriksson, and S. Coppersmith, A decoherence-free subspace in a charge quadrupole qubit, *Nature communications* **8**, 15923 (2017).
- [42] L. Chirolli and G. Burkard, Decoherence in solid-state qubits, *Advances in Physics* **57**, 225 (2008).
- [43] D. Klauser, W. Coish, and D. Loss, Nuclear spin state narrowing via gate-controlled rabi oscillations in a double quantum dot, *Physical Review B—Condensed Matter and Materials Physics* **73**, 205302 (2006).
- [44] G. Tosi, F. A. Mohiyaddin, V. Schmitt, S. Tenberg, R. Rahman, G. Klimeck, and A. Morello, Silicon quantum processor with robust long-distance qubit couplings, *Nature communications* **8**, 450 (2017).
- [45] M. D. Shulman, S. P. Harvey, J. M. Nichol, S. D. Bartlett, A. C. Doherty, V. Umansky, and A. Yacoby, Suppressing qubit dephasing using real-time hamiltonian estimation, *Nature communications* **5**, 5156 (2014).
- [46] J. M. Nichol, L. A. Orona, S. P. Harvey, S. Fallahi, G. C. Gardner, M. J. Manfra, and A. Yacoby, High-fidelity entangling gate for double-quantum-dot spin qubits, *npj Quantum Information* **3**, 3 (2017).
- [47] L. A. Orona, J. M. Nichol, S. P. Harvey, C. G. Böttcher, S. Fallahi, G. C. Gardner, M. J. Manfra, and A. Yacoby, Readout of singlet-triplet qubits at large magnetic field gradients, *Physical Review B* **98**, 125404 (2018).
- [48] A. Sigillito, M. Gullans, L. Edge, M. Borselli, and J. Petta, Coherent transfer of quantum information in a silicon double quantum dot using resonant swap gates, *npj Quantum Information* **5**, 110 (2019).
- [49] K. Takeda, A. Noiri, J. Yoneda, T. Nakajima, and S. Tarucha, Resonantly driven singlet-triplet spin qubit in silicon, *Physical Review Letters* **124**, 117701 (2020).
- [50] K. Tsoukalas, U. von Lüpke, A. Orekhov, B. Hetényi, I. Seidler, L. Sommer, E. G. Kelly, L. Massai, M. Aldeghi, M. Pita-Vidal, *et al.*, A dressed singlet-triplet qubit in germanium, *arXiv preprint arXiv:2501.14627* (2025).
- [51] M. P. Wardrop and A. C. Doherty, Exchange-based two-qubit gate for singlet-triplet qubits, *Physical Review B* **90**, 045418 (2014).
- [52] M. D. Shulman, O. E. Dial, S. P. Harvey, H. Bluhm, V. Umansky, and A. Yacoby, Demonstration of entanglement of electrostatically coupled singlet-triplet qubits, *science* **336**, 202 (2012).
- [53] H. Qiao, Y. P. Kandel, J. S. V. Dyke, S. Fallahi, G. C. Gardner, M. J. Manfra, E. Barnes, and J. M. Nichol, Floquet-enhanced spin swaps, *Nature communications* **12**, 2142 (2021).
- [54] D. Loss and D. P. DiVincenzo, Quantum computation with quantum dots, *Physical Review A* **57**, 120 (1998).
- [55] I. Heinz, A. R. Mills, J. R. Petta, and G. Burkard, Analysis and mitigation of residual exchange coupling in linear spin-qubit arrays, *Physical Review Research* **6**, 013153 (2024).
- [56] I. Heinz and G. Burkard, Crosstalk analysis for simultaneously driven two-qubit gates in spin qubit arrays, *Physical Review B* **105**, 085414 (2022).
- [57] I. Heinz and G. Burkard, Crosstalk analysis for single-qubit and two-qubit gates in spin qubit arrays, *Physical Review B* **104**, 045420 (2021).
- [58] B. Undseth, X. Xue, M. Mehmandoust, M. Rimbach-Russ, P. T. Eendebak, N. Samkharadze, A. Sammak, V. V. Dobrovitski, G. Scappucci, and L. M. Vandersypen, Nonlinear response and crosstalk of electrically driven silicon spin qubits, *Physical Review Applied* **19**, 044078 (2023).
- [59] C. Volk, A.-M. J. Zwerver, U. Mukhopadhyay, P. T. Eendebak, C. J. van Diepen, J. P. Dehollain, T. Hensgens, T. Fujita, C. Reichl, W. Wegscheider, *et al.*, Loading a quantum-dot based “qubyte” register, *npj Quantum Information* **5**, 29 (2019).
- [60] A. Mills, M. Feldman, C. Monical, P. Lewis, K. Larson, A. Mounce, and J. R. Petta, Computer-automated tuning procedures for semiconductor quantum dot arrays, *Applied Physics Letters* **115** (2019).
- [61] E. G. Kelly, A. Orekhov, N. W. Hendrickx, M. Mergenthaler, F. J. Schupp, S. Paredes, R. S. Eggli, A. V. Kuhlmann, P. Harvey-Collard, A. Fuhrer, *et al.*, Capacitive crosstalk in gate-based dispersive sensing of spin qubits, *Applied Physics Letters* **123** (2023).
- [62] D. C. McKay, C. J. Wood, S. Sheldon, J. M. Chow, and J. M. Gambetta, Efficient z gates for quantum computing, *Physical Review A* **96**, 022330 (2017).
- [63] S. Mehl, H. Bluhm, and D. P. DiVincenzo, Two-qubit couplings of singlet-triplet qubits mediated by one quantum state, *Physical Review B* **90**, 045404 (2014).
- [64] H. Qiao, Y. P. Kandel, S. Fallahi, G. C. Gardner, M. J. Manfra, X. Hu, and J. M. Nichol, Long-distance superexchange between semiconductor quantum-dot electron spins, *Physical Review Letters* **126**, 017701 (2021).
- [65] E. J. Connors, J. Nelson, H. Qiao, L. F. Edge, and J. M. Nichol, Low-frequency charge noise in si/sige quantum dots, *Physical Review B* **100**, 165305 (2019).
- [66] E. J. Connors, J. Nelson, L. F. Edge, and J. M. Nichol, Charge-noise spectroscopy of si/sige quantum dots via dynamically-decoupled exchange oscillations, *Nature communications* **13**, 940 (2022).
- [67] F. Ye, A. Ellaboudy, D. Albrecht, R. Vudatha, N. T. Jacobson, and J. M. Nichol, Characterization of individual charge fluctuators in si/sige quantum dots, *Physical Review B* **110**, 235305 (2024).
- [68] B. M. Freeman, J. S. Schoenfeld, and H. Jiang, Comparison of low frequency charge noise in identically patterned si/sio2 and si/sige quantum dots, *Applied Physics Letters* **108** (2016).
- [69] P. Zhao, P. Xu, D. Lan, J. Chu, X. Tan, H. Yu, and Y. Yu, High-contrast zz interaction using superconducting qubits with opposite-sign anharmonicity, *Physical Review Letters* **125**, 200503 (2020).
- [70] A. Pan, T. E. Keating, M. F. Gyure, E. J. Pritchett, S. Quinn, R. S. Ross, T. D. Ladd, and J. Kerckhoff, Resonant exchange operation in triple-quantum-dot qubits for spin-photon transduction, *Quantum Science and Technology* **5**, 034005 (2020).
- [71] H. Y. Waleign, X. Cai, B. Li, E. Barnes, and J. M. Nichol, Dynamically corrected gates in silicon singlet-triplet spin qubits, *Physical Review Applied* **22**, 064029 (2024).
- [72] N. Lambert, E. Giguère, P. Menczel, B. Li, P. Hopf, G. Suárez, M. Gali, J. Lishman, R. Gadhvi, R. Agarwal, *et al.*, Qutip 5: The quantum toolbox in python, *arXiv preprint arXiv:2412.04705* (2024).
- [73] J. Duan, P. Shi, and F. Yan, [Qusim: A object-oriented](#)

- software toolkit for qubits simulation and control (2024).
- [74] Y.-C. Yang, S. Coppersmith, and M. Friesen, Achieving high-fidelity single-qubit gates in a strongly driven charge qubit with $1/f$ charge noise, *npj Quantum Information* **5**, 12 (2019).
- [75] M. Rimbach-Russ, S. G. Philips, X. Xue, and L. M. Vandersypen, Simple framework for systematic high-fidelity gate operations, *Quantum Science and Technology* **8**, 045025 (2023).
- [76] D. A. Rower, L. Ding, H. Zhang, M. Hays, J. An, P. M. Harrington, I. T. Rosen, J. M. Gertler, T. M. Hazard, B. M. Niedzielski, *et al.*, Suppressing counter-rotating errors for fast single-qubit gates with fluxonium, *PRX Quantum* **5**, 040342 (2024).
- [77] V. E. Manucharyan, J. Koch, L. I. Glazman, and M. H. Devoret, Fluxonium: Single cooper-pair circuit free of charge offsets, *Science* **326**, 113 (2009).
- [78] W. Magnus, On the exponential solution of differential equations for a linear operator, *Communications on pure and applied mathematics* **7**, 649 (1954).
- [79] M. F. Zwanenburg, S. Singh, E. Y. Huang, F. Yilmaz, T. V. Stefanski, J. Hu, P. Kumaravadivel, and C. K. Andersen, Single-qubit gates beyond the rotating-wave approximation for strongly anharmonic low-frequency qubits, *arXiv preprint arXiv:2503.08238* (2025).
- [80] X. Zhang, E. Morozova, M. Rimbach-Russ, D. Jirovec, T.-K. Hsiao, P. C. Fariña, C.-A. Wang, S. D. Oosterhout, A. Sammak, G. Scappucci, *et al.*, Universal control of four singlet–triplet qubits, *Nature Nanotechnology* **20**, 209 (2025).
- [81] A. Mills, C. Guinn, M. Feldman, A. Sigillito, M. Gullans, M. Rakher, J. Kerckhoff, C. Jackson, and J. Petta, High-fidelity state preparation, quantum control, and readout of an isotopically enriched silicon spin qubit, *Physical Review Applied* **18**, 064028 (2022).
- [82] Y. Sung, L. Ding, J. Braumüller, A. Vepsäläinen, B. Kannan, M. Kjaergaard, A. Greene, G. O. Samach, C. McNally, D. Kim, *et al.*, Realization of high-fidelity cz and zz-free iswap gates with a tunable coupler, *Physical Review X* **11**, 021058 (2021).
- [83] X. Yang, J. Chu, Z. Guo, W. Huang, Y. Liang, J. Liu, J. Qiu, X. Sun, Z. Tao, J. Zhang, *et al.*, Coupler-assisted leakage reduction for scalable quantum error correction with superconducting qubits, *Physical Review Letters* **133**, 170601 (2024).
- [84] X. Xue, B. D’Anjou, T. F. Watson, D. R. Ward, D. E. Savage, M. G. Lagally, M. Friesen, S. N. Coppersmith, M. A. Eriksson, W. A. Coish, *et al.*, Repetitive quantum nondemolition measurement and soft decoding of a silicon spin qubit, *Physical Review X* **10**, 021006 (2020).
- [85] A. Kubica, A. Haim, Y. Vaknin, H. Levine, F. Brandão, and A. Retzker, Erasure qubits: Overcoming the $t \ll 1$ limit in superconducting circuits, *Physical Review X* **13**, 041022 (2023).
- [86] J. Duan, F. Torres-Leal, and J. Nichol, Figure and simulation scripts for mitigating residual exchange coupling in resonant singlet- triplet qubits, [10.5281/zenodo.17794872](https://doi.org/10.5281/zenodo.17794872) (2025).
- [87] E. Kawakami, T. Jullien, P. Scarlino, D. R. Ward, D. E. Savage, M. G. Lagally, V. V. Dobrovitski, M. Friesen, S. N. Coppersmith, M. A. Eriksson, *et al.*, Gate fidelity and coherence of an electron spin in an si/sige quantum dot with micromagnet, *Proceedings of the National Academy of Sciences* **113**, 11738 (2016).
- [88] J. Poyatos, J. I. Cirac, and P. Zoller, Complete characterization of a quantum process: the two-bit quantum gate, *Physical Review Letters* **78**, 390 (1997).
- [89] M. A. Nielsen, A simple formula for the average gate fidelity of a quantum dynamical operation, *Physics Letters A* **303**, 249 (2002).
- [90] L. H. Pedersen, N. M. Møller, and K. Mølmer, Fidelity of quantum operations, *Physics Letters A* **367**, 47 (2007).
- [91] S. Harvey, C. Böttcher, L. Orona, S. Bartlett, A. Doherty, and A. Yacoby, Coupling two spin qubits with a high-impedance resonator, *Physical Review B* **97**, 235409 (2018).
- [92] H. H. Kang, I. T. Rosen, M. Hays, J. A. Grover, and W. D. Oliver, Remote entangling gates for spin qubits in quantum dots using a charge-sensitive superconducting coupler, *Physical Review Applied* **23**, 044055 (2025).